A variable temperature solid-state nuclear magnetic resonance, electron paramagnetic resonance and Raman scattering study of molecular dynamics in ferroelectric fluorides

A variable temperature solid-state nuclear magnetic resonance, electron paramagnetic resonance and Raman scattering study of molecular dynamics in ferroelectric fluorides

Radoslaw M Kowalczyk[1,2,3]**, Thomas F Kemp**[1]**, David Walker**[1]**, Kevin J Pike**[1]**, Pamela A Thomas**[1]**, Jens Kreisel**[2]**, Ray Dupree**[1]**, Mark E Newton**[1]**, John V Hanna**[1] **and Mark E Smith**[1]

[1] Department of Physics, University of Warwick, Gibbet Hill Road, Coventry CV4 7AL, UK
[2] Laboratoire des Matériaux et du Génie Physique, Miniatec, CNRS, Grenoble Institute of Technology, 3 parvis Louis Néel, 38016 Grenoble, France

E-mail: r.kowalczyk@surrey.ac.uk

Abstract

The local nuclear and electronic structures and molecular dynamics of the ferroelectric lattice in selected geometric fluorides ($BaMgF_4$, $BaZnF_4$, $BaMg_{1-x}Mn_xF_4$ and $BaMg_{1-x}Ni_xF_4$; $x = 0.001$ and 0.005) have been investigated. The ^{19}F and ^{25}Mg isotropic chemical shift δ_{iso}, ^{25}Mg quadrupolar coupling constants (C_q) and asymmetry parameters (η) reflect the geometry of the coordination spheres. The zero-field splitting parameters $|D|$ and $|E|$ are consistent with distorted axial symmetry (low temperatures) and nearly rhombic symmetry (high temperatures) of octahedral Mn^{2+} coordination. The high resolution of the nuclear magnetic resonance, electron paramagnetic resonance and phonon spectra are consistent with the highly ordered crystallographic structure. Combined multi-technique data evidence the subtle discontinuous changes in the temperature dependences of $|D|$ and $|E|$, isotropic chemical shifts δ_{iso} and signature parameters of Raman bands and suggest a discontinuous structural distortion of the fluoride octahedra. The temperature at which this change occurs depends on the ionic radius of the central ion of the octahedral site and is estimated to be $\sim$300 K for Zn^{2+} fluorides and $\sim$240 K for Mg^{2+} fluorides. This geometrical distortion modifies the lattice dynamics and originates from the rotation of the fluoride octahedra around a new direction approximately perpendicular to that related to the paraelectric–ferroelectric phase transition.

S Online supplementary data available from stacks.iop.org/JPhysCM/23/315402/mmedia

1. Introduction

Ferroelectrics and ferromagnets are of great technological importance and their properties are intimately determined by their structure and the dynamics at the atomic and molecular levels [1–3]. In multiferroic materials, electric and magnetic orders coexist and can interact [4], despite the fact that the well accepted mechanisms of electric and magnetic orderings have been regarded in the past as mutually exclusive [5]. Some multiferroics combine new types of ferroelectricity, as for instance in geometrical ferroelectrics (where electric polarization arises as a consequence of atom shifts and structural distortions) together with magnetism [6, 7].

Despite a recent resurgence of interest in geometric ferroelectrics, our understanding of the molecular dynamics

[3] Present address: Department of Physics, University of Surrey, Guildford GU2 7XH, UK. Author to whom any correspondence should be addressed.

in such ferroelectrics remains limited [8]. In particular, the influence of geometric distortions on the lattice dynamics deserves further experimental attention, as these are often related to the cation displacement responsible for electric polarization [9]. One of the most intensively discussed problems is that of the nature of the coupling between the magnetism and the lattice dynamics [10]. In this investigation magnetic ions are present both as dilute dopants and as the ions responsible for magnetic ordering in the sample. An improved understanding of the molecular dynamics is also crucial to the understanding of the stability of the polarization and magnetization in multiferroics with geometric ferroelectricity, which could potentially result in greater macroscopic control of both magnetic and electric orders being achieved in these systems [11].

Ferroelectric, optical and multiferroic properties of geometric fluorides have been studied and characterized in detail previously [12–17]. This study focuses on the diamagnetic members of the $BaMF_4$ family (M^{2+} = Mn^{2+}, Fe^{2+}, Co^{2+}, Ni^{2+}, Cr^{2+}, Zn^{2+}, Mg^{2+}), namely $BaMgF_4$ and $BaZnF_4$. They were subsequently doped with Mn^{2+} and Ni^{2+} ions to introduce paramagnetic probes, identical to those responsible for magnetism in $BaMnF_4$ and $BaNiF_4$, and to allow other studies to be facilitated [18, 19]. For three members of the $BaMF_4$ family, namely $BaMnF_4$, $BaCoF_4$ and $BaNiF_4$, multiferroic properties were reported and are now widely accepted [13–15]. The molecular dynamics of geometric fluorites has also attracted attention, but most studies are limited to understanding the origin of spontaneous polarization and the paraelectric–ferroelectric phase transition, which is predicted to occur around 100 K above the melting point (in the range of 990–1240 K, respectively for $BaFeF_4$ to $BaNiF_4$) [20, 21]. The low temperature studies have been predominantly focused on magnetic properties of $BaMnF_4$ and $BaNiF_4$ [12, 15, 22, 23]. The incommensurate–commensurate phase transition, which occurs at 250 K, has been observed and accepted only for $BaMnF_4$ [12, 24]. Only recently have the low temperature dynamics of $BaZnF_4$ and $BaMn_{1-x}Zn_xF_4$ ($0 < x < 0.25$) been studied and analysed in more detail [25–28].

Magnetic resonance techniques have been somewhat rarely used to study these fluorides, despite the possibility of providing information on the temperature dependence of the crystal field induced by the lattice dynamics [12, 29]. Solid-state ^{19}F NMR was used to provide a reference for quantum mechanical calculation of the chemical shifts in fluorides [30], whereas EPR studies have been focused on the characterization of properties and the coordination sphere of paramagnetic ions in the lattice [31, 32]. Only one study used paramagnetic Mn^{2+} as a probe doped in a $BaMgF_4$ matrix [33]. The directions of the zero-field splitting (ZFS) tensor, evaluated at a few temperatures, were used to define and to monitor an order parameter for the paraelectric–ferroelectric phase transition and to estimate the Curie temperature [33]; however, the low temperature molecular dynamics and the direct dependence of the ZFS on temperature were not explored [33].

Raman experiments were also mostly focused on the ferroelectric–paraelectric phase transition [12, 34] and the incommensurate–commensurate phase transition in $BaMnF_4$

[24]. Detailed data over a wide range of temperatures have been published only for $BaZnF_4$ and there are reports of anomalous behaviour for some particular modes at 300 K [25]. Such behaviour was interpreted as dynamic order–disorder changes, while a phase transition does not occur [25–27]. This hypothesis has attracted some attention and studies of $BaMn_{1-x}Zn_xF_4$ ($0 < x < 0.25$) soon followed, but without providing a definitive model [28].

The motivation of this work is to extend the knowledge and understanding of the lattice dynamics in geometric ferroelectrics using a variable temperature approach for a suite of different experimental methods. Solid-state nuclear magnetic resonance (solid-state NMR) and electron paramagnetic resonance (EPR) provide local nuclear and electronic probes of the lattice in different microenvironments in each system, while Raman scattering captures the characteristics of local correlations of phonons. The choice of these techniques is justified by their past successful application to the study of the molecular dynamics and phase transitions in a variety of inorganic materials [35–37]. They also provide the possibility of studying a comprehensive set of materials including diamagnetic (NMR), magnetically dilute (EPR) and magnetic samples (Raman) [38–40]. This study re-examines data for $BaZnF_4$ (NMR and Raman) and extends the study to $BaZn_{0.999}Mn_{0.001}F_4$ (EPR) to obtain a picture of molecular dynamic changes over a wide range of temperatures. To explore further the low temperature molecular dynamics, the main studies of this work have been focused on $BaMgF_4$, $BaMg_{0.999}Mn_{0.001}F_4$, $BaMg_{0.995}Mn_{0.005}F_4$, and $BaMg_{0.995}Ni_{0.005}F_4$ (NMR, EPR, Raman extended to energies above 200 cm^{-1}). Indeed, if the situation in fluorites is universal, as suggested in [25], dynamic order should also be even more apparent in $BaMgF_4$ because of the lower level of structural distortion due to the smaller radius of Mg^{2+} compared to Zn^{2+}.

This paper reports experimental data that favour a discontinuous change in the structural distortion of fluoride octahedra based on the observed temperature dependence of the zero-field splitting parameters $|D|$ and $|E|$ extracted from EPR spectra. These changes are supported by discontinuities in the temperature dependence of the isotropic chemical shift δ_{iso} in variable temperature solid-state magic angle spinning (MAS) NMR spectra, and by the changes observed in frequencies and linewidths of some high frequency bands in the Raman spectra. This geometrical change is expected to play an important role in modifying the lattice dynamics as an initial step in the creation of dynamic order in the structure.

2. Experimental procedures

2.1. Synthesis and structure

$BaMgF_4$ and $BaZnF_4$ were synthesized by reacting mixtures of fine powders of binary compounds (BaF_2 and MgF_2 or ZnF_2) in graphite crucibles under an Ar atmosphere. The synthesis temperature was about 50–100 K above the melting point of $BaMgF_4$ or $BaZnF_4$ but below the melting point of the reactants. The best samples were obtained by allowing

48 h for the reaction followed by a slow cooling at a rate of 2 K h^{-1}. The reaction time and cooling rate were carefully controlled to avoid the creation of different temperature-related phases because there was a narrow temperature window for synthesis. These synthesis conditions led to a shell containing small single crystals. The outer layer of the shell contained a small amount of oxide impurities as a result of the reaction of water trapped in MgF$_2$ or especially in the highly hygroscopic ZnF$_2$. Only single crystals from the inside shell were selected as samples of appropriate purity.

The synthesized prototype compounds BaMgF$_4$ and BaZnF$_4$ were subsequently doped with a low level (0.1% and 0.5%) of paramagnetic Mn^{2+} and Ni^{2+} ions, which substitute for the Mg^{2+} and Zn^{2+} ions in the structure [31]. The synthesis temperature of the doped compounds was adjusted to reflect the lower or higher melting temperature of MnF$_2$ and NiF$_2$ but the general procedure was identical to that used for BaMgF$_4$ or BaZnF$_4$.

The crystallographic structures of the synthesized materials were found to be orthorhombic with space group $Cmc2_1$ (by means of both single-crystal and powder x-ray diffraction—XRD) in agreement with previously reported data [18, 41].

2.2. Solid-state static and magic angle spinning (MAS) nuclear magnetic resonance (NMR)

Room temperature solid-state MAS NMR measurements were performed on a Bruker Avance II 500 MHz (11.7 T) spectrometer. A high speed 2.5 mm rotor Bruker MAS fluorine-background-free probe, tuned to 470.39 MHz, was used in association with this spectrometer. All spectra were referenced to an external standard polytetrafluoroethylene (PTFE) at −123.2 ppm. A pulse sequence with a single 90° pulse of 4.5 μs was used. A typical signal consists of 64 averaged acquisitions. The delay time between acquisitions was typically 5 s. The spinning rates were varied between 8 and 30 kHz. Variable temperature solid-state MAS NMR measurements were carried out on Varian 600 MHz (14.1 T) spectrometer. A specially made low temperature Doty Scientific MAS NMR probe, tuned to 564.29 MHz, was used with this spectrometer. A pulse sequence with a single 90° pulse of 6.0 μs was used. A typical signal consists of 16 averaged acquisitions. Spectra were recorded in the temperature range 120–310 K. The delay time between acquisitions is typically 10–30 s depending on the temperature. The spinning rates varied from 8 to 16 kHz, from low temperature to room temperature respectively.

Static broadline ^{25}Mg NMR data were acquired at ambient temperature (292 K) and at 150 K using a Varian 600 MHz (14.1 T) spectrometer operating at a ^{25}Mg Larmor frequency of 36.72 MHz. A Bruker static NMR probe with a 10 mm diameter coil was used with a flow of nitrogen gas to cool the sample. Spectra were acquired with a pulse sequence $\theta_{\pi/2} - \tau - \theta_{\pi} - \tau_1$ (FID acquisition) [42, 43]. A non-selective $\pi/2$ pulse width of 15 μs ($\gamma_{Mg}B_1/2\pi = 16.7$ kHz) was calibrated using solid MgO and used to calculate selective 'solid' pulses, with $\theta_{\pi/2} = 4$ μs and $\theta_{\pi} = 8$ μs used for experiments at

both temperatures. The τ echo delay was 50 μs. 8000 FID transients were averaged at 292 K with 20 s relaxation delays and 80 were averaged at 150 K with 120 s delays. The spectra were referenced using the ^{25}Mg resonance at 26 ppm for solid MgO at 292 K.

All solid-state MAS NMR spectra were simulated using the free-distribution simulation program SIMPSON [44]. Quantum mechanical calculations of chemical shifts and chemical shift anisotropies were carried out using plane-wave basis sets and periodic boundary conditions based on experimental XRD data (CASTEP [45]). The calculated values of chemical shielding were referenced (uniformly shifted), to fit the best experimental results.

2.3. Electron paramagnetic resonance (EPR)

The variable temperature continuous wave electron paramagnetic resonance (EPR) experiments were performed using a Bruker EMX spectrometer consisting of an electromagnet and an X-band (9.450 GHz) microwave bridge ER 041XG with a Bruker ER4105D double rectangular resonator. A helium gas flow cryostat was used and the temperature was varied in the range 5–300 K (±1 K) by an Oxford Instruments auto-tuning temperature controller ITC503. Control experiments were carried out with a Bruker ER 4102ST rectangular resonator with a nitrogen gas flow cryostat in the temperature range 120–360 K, monitored by an Oxford Instruments auto-tuning temperature controller. High temperature experiments in the range 300–670 K were performed using a modified Bruker high temperature cavity and nitrogen gas flow system. The Q-band (32.28 GHz) EPR spectra were recorded using a Bruker ELEXYS spectrometer and SuperQ-FT microwave bridge in conjunction with a Bruker Q-band EN517D2 resonator. All spectra were recorded with 100 kHz modulation frequency and modulation amplitudes in the range 0.1–0.3 mT, with the exception of the high temperature measurements where the maximum available modulation amplitude (0.02 mT) was applied. A typical microwave power of 1.00 mW was used at which no saturation effects were observed. All EPR spectra were simulated using the EASYSPIN simulation package [46].

2.4. Raman spectroscopy

Raman spectra were recorded in a back-scattering geometry using a LabRam Jobin-Yvon spectrometer with a spectral resolution of about 0.2 cm^{-1} and a Rayleigh scattering cut-off at 80 cm^{-1} with Notch filter. The beam of an Ar$^+$ ion laser of 488 nm wavelength was focused to a 1 μm^2 spot through a times 50 long focal objective. All experiments were performed with a typical incident power of 4–8 mW, after verification that this power level does not incur sample damage. Temperature-dependent measurements were carried out on selected good quality fluoride crystals by using a commercial Linkam cooling/heating stage and were conducted upon heating with a typically slow rate of 10 K min^{-1}. The deconvolution of the Raman spectra was performed using the LabSpec software.
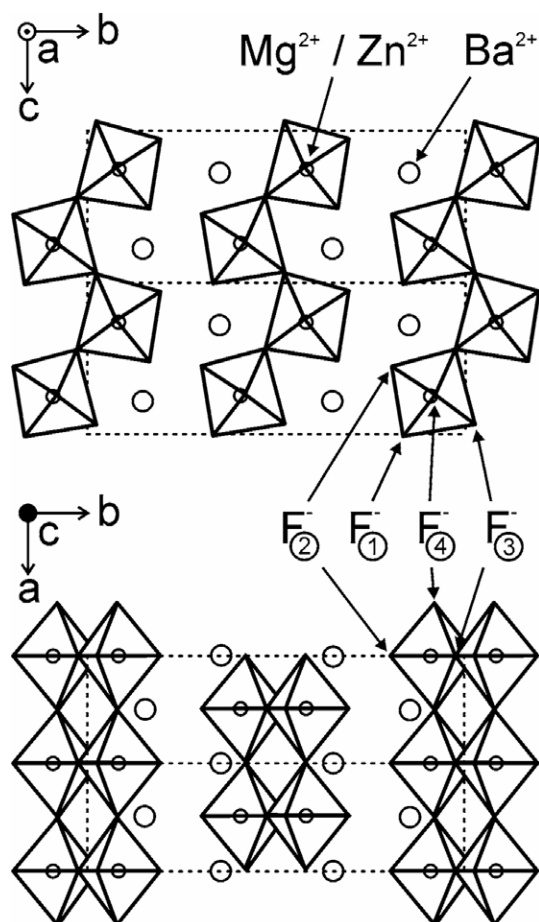
Figure 1. The schematic structure of $BaMgF_4$ and $BaZnF_4$. Fluorine atoms form a distorted octahedron, which surrounds Mg^{2+}/Zn^{2+} ions. Ba^{2+} ions lie between chains of rotated octahedra. The four fluorine nuclei per unit cell are labelled.

3. Results and discussion

The microstructure of $BaMF_4$ (M^{2+} = Mn^{2+}, Fe^{2+}, Co^{2+}, Ni^{2+}, Cr^{2+}, Zn^{2+}, Mg^{2+}) consists of a network of octahedra with a central M^{2+} ion and six nearest neighbour fluorine ligand ions as shown schematically in figure 1. Ba^{2+} ions are located in the cavities between octahedra (figure 1). The metal–fluorine distances range from 2.60 to 3.00 Å for (Ba^{2+}–F^-) and from 1.93 to 2.07 Å for (M^{2+}–F^-) [18, 19].

3.1. ^{19}F and ^{25}Mg nuclear magnetic resonance (NMR)

The room temperature ^{19}F solid-state MAS NMR spectra of diamagnetic $BaZnF_4$ and $BaMgF_4$ acquired at 470.39 MHz (11.74 T) with a spinning frequency of 30 kHz are presented in figures 2(a) and (b) respectively, with the elucidated isotropic chemical shifts (δ_{iso}) collected in table 1. Each spectrum consists of four peaks which can be attributed to the four inequivalent fluorine nuclei in the unit cell (see figure 1). The upfield ^{19}F shifts (producing negative δ_{iso} values) reflect a significant presence of additional electron density on each fluorine atom, thus corresponding to the highly ionic character of these systems [47].
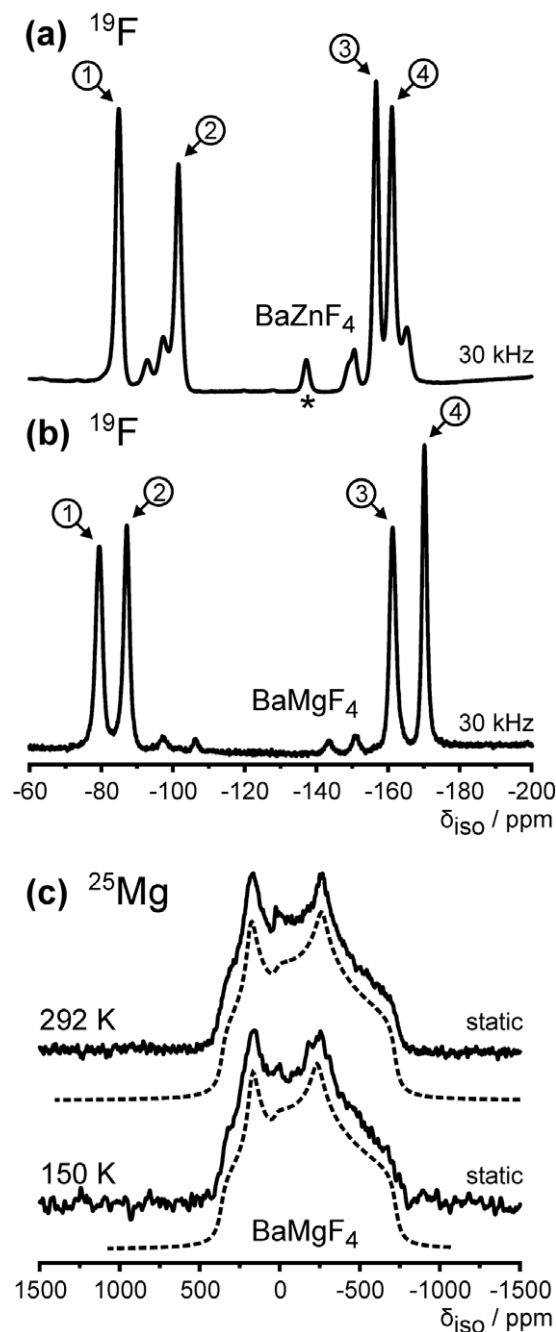

Figure 2. ^{19}F solid-state MAS NMR spectra of $BaZnF_4$ (a) and $BaMgF_4$ (b) recorded at room temperature with observed peaks attributed to different fluorine nuclei in the unit cell (for their relation to the structure see figure 1). An asterisk denotes an impurity; all other unnumbered peaks are spinning side bands. Also shown are ^{25}Mg NMR spectra of $BaMgF_4$ (c) recorded at 292 and 150 K with their simulations (dashed lines).

GIPAW DFT calculations of the ^{19}F isotropic chemical shifts using the CASTEP code [45] (see table 1) show that calculated δ_{iso} values exhibit general agreement with the experimental measurements. This computational tool also confirmed the assignment of all ^{19}F δ_{iso} to the appropriate fluorine nuclei of the crystallographic structure as presented in figure 1.

Table 1. Experimental and calculated (CASTEP [45]) ^{19}F NMR chemical shifts (δ_{iso}) for $BaZnF_4$ and $BaMgF_4$.

		$\delta_{iso}^{F(1)}$/ppm	$\delta_{iso}^{F(2)}$/ppm	$\delta_{iso}^{F(3)}$/ppm	$\delta_{iso}^{F(4)}$/ppm
$BaZnF_4$	Experiment	−84.8	−101.5	−156.6	−161.0
	Calculation	−101	−104	−160	−181
$BaMgF_4$	Experiment	−79.4	−87.0	−161.1	−170.1
	Calculation	−75	−85	−168	−179

As the main contribution to chemical shift arises from interactions with all the nearest neighbouring atoms, the differences in δ_{iso} are directly related to distinctive fluorine coordinations between shared (fluorine nuclei F(3) and F(4) in figure 1, with two M^{2+} in the chain) and non-shared (fluorine nuclei F(1) and F(2) in figure 1, with a metal M^{2+} only on one side) positions in the fluoride octahedra. The differences in δ_{iso} between F(1) and F(2), as well as F(3) and F(4), are more likely to be due to the differing numbers of barium atoms in the coordination sphere and the very different local geometries caused by this. The shift differences reported between all the sets of sites are in good agreement with previous ^{19}F measurements [30, 48], with the shifts here being reported with higher precision as a result of the higher field and faster spinning applied.

The relative differences in δ_{iso} between $BaZnF_4$ and $BaMgF_4$ are a consequence of the more electronegative character of Mg^{2+} compared to Zn^{2+}, which then produces the more ionic character of $BaMgF_4$, and the difference in ionic radius between Mg^{2+} ($r = 0.69$ Å) and Zn^{2+} ($r = 0.74$ Å), which is in turn related to the more distorted octahedra in $BaZnF_4$ at room temperature.

Representative variable temperature solid-state ^{19}F MAS NMR spectra of $BaMgF_4$ are shown in figures 3(a) and (a′) (for $BaZnF_4$ spectra see figure SM2 in supplementary material SM.1 available at stacks.iop.org/JPhysCM/23/315402/mmedia). They have complicated structures which arise from the presence of four fluorine signals with significant chemical shift anisotropies (CSA) and the presence of strong background signals in the low temperature probe (see figure 3(a)). However, application of the procedure described in detail in supplementary material SM.1 (available at stacks.iop.org/JPhysCM/23/315402/mmedia) allowed unambiguous identification and monitoring of δ_{iso} as a function of temperature with good precision (±2 ppm).

At each temperature point, all independent δ_{iso} (for each fluorine in the unit cell) were found from the spectral simulation using SIMPSON [43]. For further analysis the differences in chemical shift (defined as $\Delta\delta_{iso}^{ij} = |\delta_{iso}^{F(i)} - \delta_{iso}^{F(j)}|$, where the fluorine nucleus (i) is labelled F(i) and i, $j = 1–4$) were taken to eliminate any temperature shifts not related to the changes in the structure. The temperature dependence of $\Delta\delta_{iso}^{ij}$ for $BaMgF_4$ is presented in figure 3(b), with that for $BaZnF_4$ in the supplementary material figure SM1 (available at stacks.iop.org/JPhysCM/23/315402/mmedia).

The values of $\Delta\delta_{iso}^{ij}$ change only slightly over the temperature range 130–310 K, as shown in figure 3(b) and figure SM2(b) (available at stacks.iop.org/JPhysCM/23/315402/mmedia). This suggests that: (i) continuous deformation of the octahedron has only a very minor effect on δ_{iso} and (ii) its dependence on the phonon dynamics can be neglected. In contrast to the case for $BaZnF_4$, for $BaMgF_4$, the discontinuity in $\Delta\delta_{iso}^{ij}$ at ∼210–220 K is observed (compare graphs in figure SM2(b) (available at stacks.iop.org/JPhysCM/23/315402/mmedia) and figure 3(b)) and it is especially evident for $\Delta\delta_{iso}^{21}$ and $\Delta\delta_{iso}^{23}$ (figure 3(b)). These $\Delta\delta_{iso}^{ij}$ correspond to chemical shifts of fluorine nuclei that are lying at the octahedra corners in a plane parallel (or close to parallel) to the *bc* crystallographic plane, where octahedra form chains separated by Ba^{2+} nuclei (figure 1).

The origin of this discontinuity lies in the discontinuous change of the fluorine coordination sphere, which is directly related to the change of the geometry of the octahedra. The largest discontinuities observed for $\Delta\delta_{iso}^{21}$ and $\Delta\delta_{iso}^{23}$ (figure 3(b)) indicate that geometrical rearrangement takes place in the plane formed by the F(1), F(2) and F(3) fluorines (figure 1). Only very minor effects are observed when F(4) is involved. A similar discontinuity in $\Delta\delta_{iso}^{ij}$ for $BaZnF_4$ has not been detected because our data were restricted to the maximum temperature achievable, 300 K (figure SM2(b) available at stacks.iop.org/JPhysCM/23/315402/mmedia).

Static broadline ^{25}Mg NMR spectra of $BaMgF_4$ acquired at 14.1 T at temperatures of 292 and 150 K are presented in figure 2(c). The well-defined quadrupolar interaction lineshape describing the (+1/2 to −1/2) central transition of the $I = 5/2$ ^{25}Mg nucleus is indicative of the highly crystalline lattice, and the short-range and long-range positional order influencing the magnesium environment [49]. At room temperature, spectral parameters ($\delta_{iso} \approx 0$ ppm, $C_q \approx$ 5.7 MHz and $\eta \approx 0.47$) are in the range typical for distorted octahedral coordination environments as reported for a number of organic and inorganic compounds [50, 51]. There exists some discrepancy between the GIPAW DFT calculated quadrupole parameters obtained using the CASTEP code ($C_q = 7.7$ MHz, $\eta = 0.51$) and the measured values reported above. Previous studies comparing calculated and measured ^{25}Mg NMR parameters have reported similar discrepancies for systems characterized by larger electric field gradients (expressed via values of C_q) [51]. This observation is ascribed to the limitations of the pseudopotentials used in these calculations.

No significant changes in spectral parameters were observed between the 292 and 150 K data (figure 2(c)), despite the potential for ^{25}Mg being a very sensitive probe of the local environment through the changes in the quadrupolar interaction [51]. However, such 'insensitivity' cannot provide definitive evidence of the high structural stability because the observed broadline spectra could mask subtle changes in the ^{25}Mg coordination. Additionally, only more detailed and systematic studies over a significantly broader range of
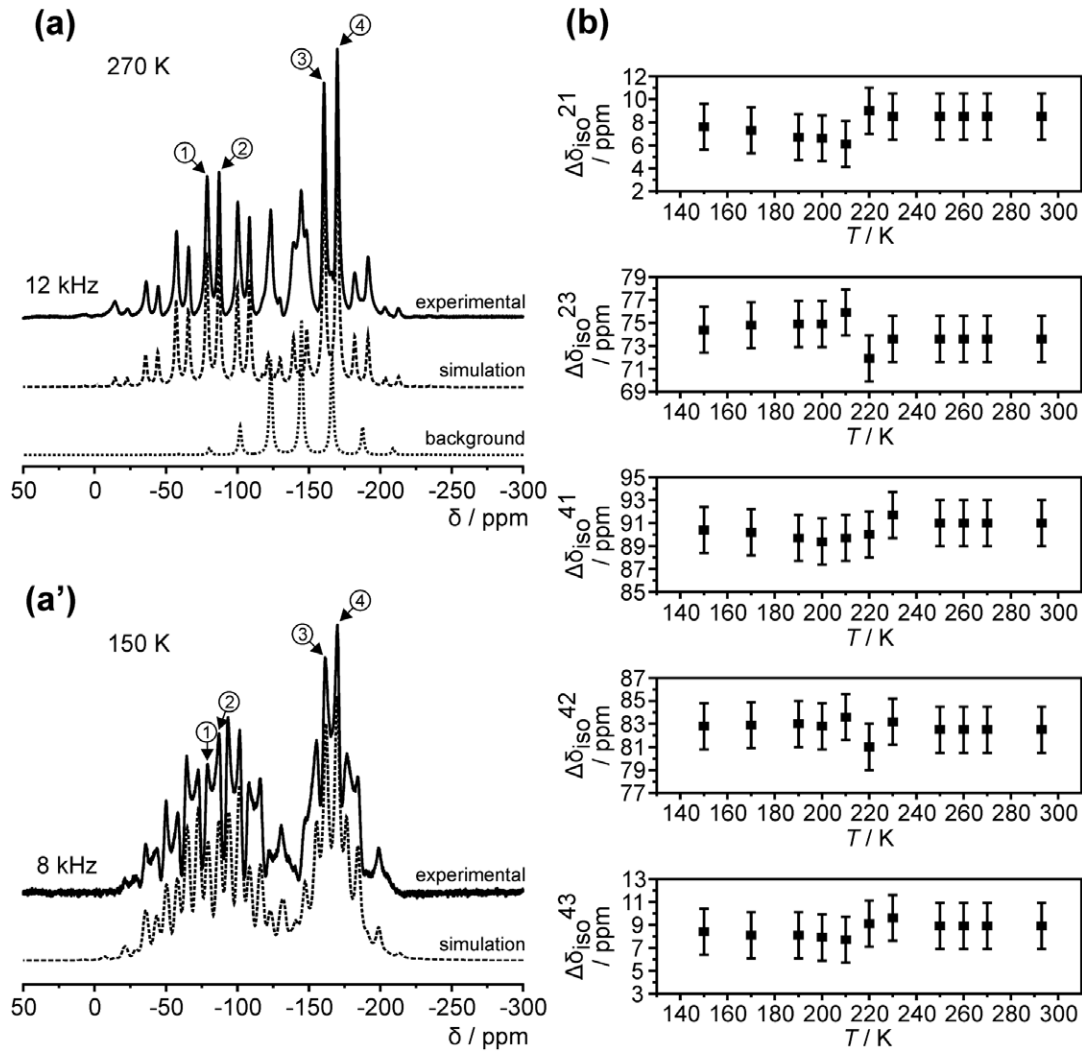
Figure 3. Variable temperature ^{19}F solid-state MAS NMR spectra of BaMgF$_4$ at 270 K (a) and 150 K (a′). The experimental spectra are given by solid lines, below which are given simulated background-free spectra (dashed lines) and simulated background components (dotted line). The δ_{iso} peaks are labelled in agreement with the structure scheme in figure 1. Also shown are temperature dependences of relative differences in chemical shifts $\Delta\delta_{iso}^{ij} = |\delta_{iso}^{F(i)} - \delta_{iso}^{F(j)}|$ ($i, j = $ 1–4) in the ^{19}F MAS NMR spectra of BaMgF$_4$ (b).

temperatures can bring definitive confirmation of the actual sensitivity of ^{25}Mg to these structure changes.

3.2. Electron paramagnetic resonance (EPR)

The X-band (9.450 GHz) EPR spectra of paramagnetic Mn^{2+} ($S = 5/2$, $I = 5/2$) doped (0.1%) into a diamagnetic BaZnF$_4$ and BaMgF$_4$ matrices are presented in figure 4(a). Remarkably well resolved structures of 30 resonances in the spectrum (five, partially overlapped, groups of six lines assigned to the allowed transitions) suggest a high level of order in the crystal structure surrounding the doped ion, which replaces the Mg^{2+} or Zn^{2+} in the dielectric matrix and has a well-defined microenvironment. The central transition ($-1/2 \rightarrow +1/2$) at $g \sim 2.00$ is split further due to a superhyperfine interaction of the unpaired electron with six fluorine nuclei ($I = 1/2$) located at the corners of fluoride octahedra (see the inset in figure 4(a) and figure 1). For other transitions this splitting is not observed due to line broadening related to ZFS.

For the higher doping levels the superhyperfine structure is not resolved because of the increased linewidth caused by dipole–dipole interactions (for details see supplementary material SM.2, figure SM3, available at stacks.iop.org/ JPhysCM/23/315402/mmedia). Such behaviour confirms the presence of the strong long-range interactions between distant Mn^{2+} ions.

The hyperfine constant for Mn^{2+} ($I = 5/2$) found from spectral simulations is $A_{iso}^{Mn} \approx 270$ MHz and the hyperfine constants for F$^-$ ($I = 1/2$) are $A_{iso}^{F} \approx 38$ and 34 MHz for BaZn$_{0.999}$Mn$_{0.001}$F$_4$ and BaMg$_{0.999}$Mn$_{0.001}$F$_4$, respectively, at room temperature. The value of the hyperfine splitting constant is in the range typical for Mn^{2+} ions [52] and depends very weakly on temperature. The small hyperfine value F$^-$ indicates a low level of delocalization of the unpaired electron spin density on the fluorines.

For BaZn$_{1-x}$Mn$_x$F$_4$ ($x = 0.001$ and 0.005), the estimated ZFS parameters are $|D| \sim 0.03$ cm^{-1} (906 MHz) and $|E| \sim 0.006$ cm^{-1} (188 MHz) at room temperature.
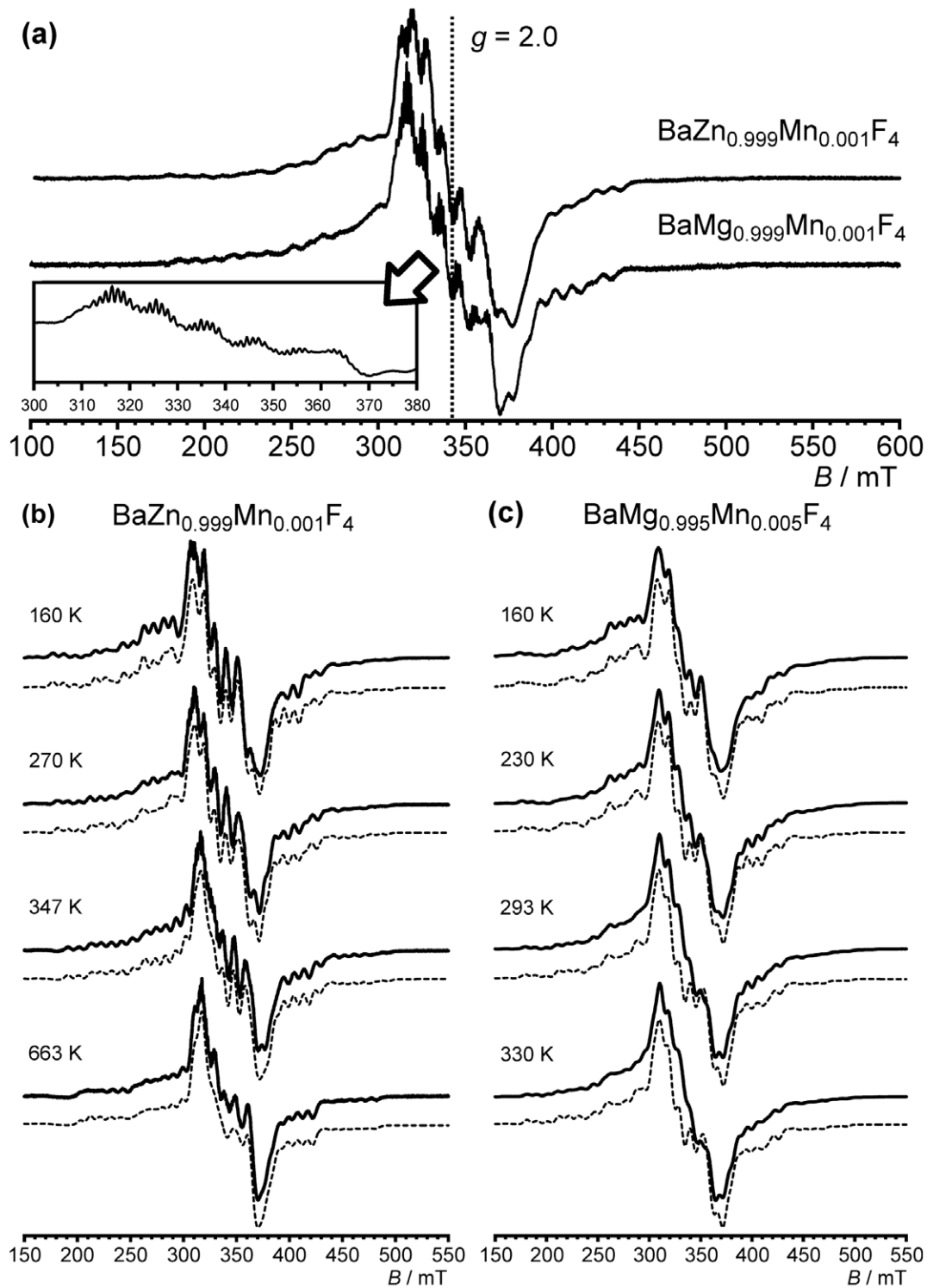
Figure 4. Room temperature X-band EPR spectra of $BaZn_{0.999}Mn_{0.001}F_4$ and $BaMg_{0.991}Mn_{0.001}F_4$ (a) with an inset showing the central part of the spectrum with superhyperfine structure. Also shown are variable temperature X-band EPR spectra and their spectral simulations (dashed line) for $BaZn_{0.999}Mn_{0.001}F_4$ (b) and $BaMg_{0.995}Mn_{0.005}F_4$ (c).

For $BaMg_{1-x}Mn_xF_4$ (x = 0.001 and 0.005), the ZFS parameters are $|D| \sim 0.03$ cm^{-1} (930 MHz) and $|E| \sim 0.006$ cm^{-1} (176 MHz) in agreement with previous single-crystal studies [33]. The ZFS parameters $|D|$ and $|E|$ provide a reliable measure of the strength of the crystal field in both

$BaZnF_4$ and $BaMgF_4$ matrices. The relatively large value of the ZFS parameter $|D|$ supports the observation that most of the electron spin density is localized on the paramagnetic ion surrounded by distorted octahedra. The ZFS parameter $|E|$ permits an assessment of the significant distortion of the crystal
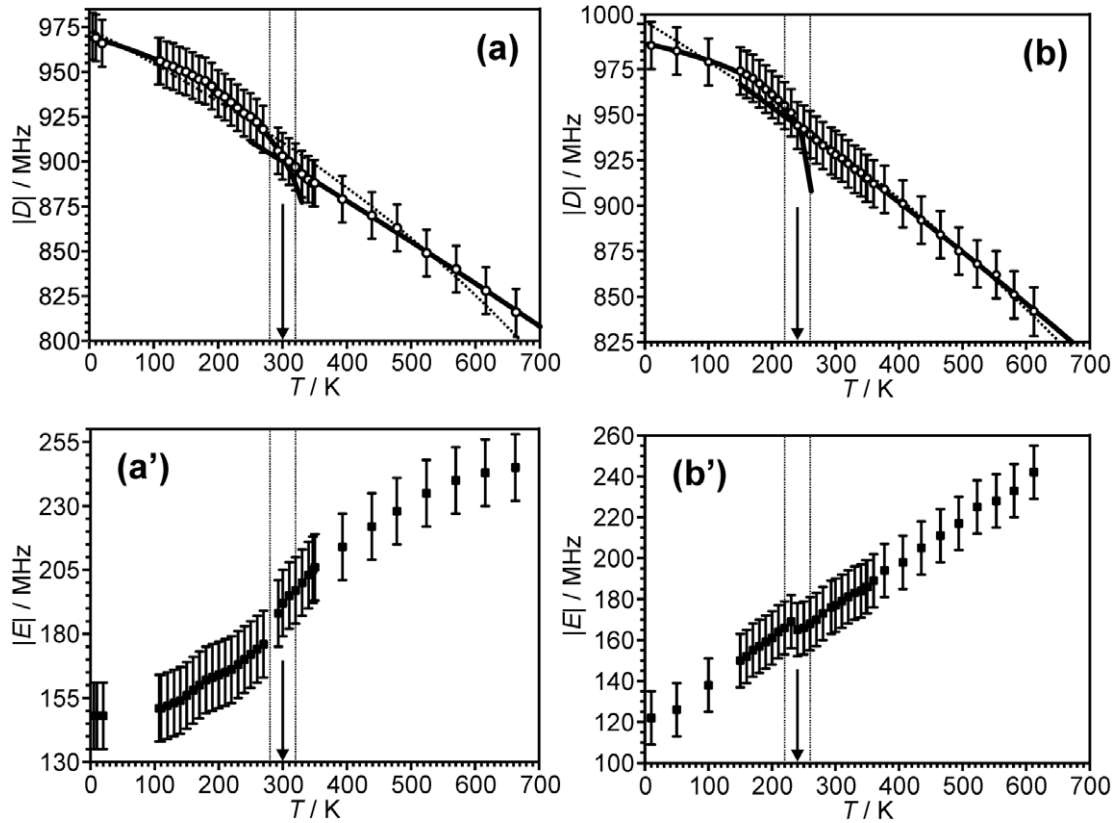
Figure 5. Temperature dependences of ZFS parameters $|D|$ ((a), (b)) and $|E|$ ((a'), (b')) for $BaZn_{0.999}Mn_{0.001}F_4$ ((a) and (a')) and for $BaMg_{0.995}Mn_{0.005}F_4$ ((b) and (b')). The $Y \propto (A_C - X)^B$ formula was used to fit the $|D|$ versus T curve over the whole temperature range (dotted lines), in the low temperature (5–240 K) region (solid lines) and in the high temperature (250–650 K) region (solid lines). Vertical dotted lines indicate the temperature range in which the discontinuity occurs.

field, which changes from distorted axial symmetry at low temperatures to nearly rhombic symmetry at high temperatures (figures 4 and 5).

The temperature evolutions of $BaZn_{0.999}Mn_{0.001}F_4$ and $BaMg_{0.995}Mn_{0.005}F_4$ spectra, together with their spectral simulations, are presented in figures 4(b) and (c). The pattern of resonances reflects allowed transitions in the spin manifolds. Changes in the linewidths, intensities and ZFS are responsible for differences between the low and high temperature spectra. The high resolution of the X-band spectra, together with the good agreement between the experiments and simulations, allowed precise estimation of the ZFS parameters $|D|$ and $|E|$. It was also possible to limit EPR experiments to X-band frequencies because more details of the spectral pattern are resolved in X-band spectra compared to Q-band spectra (for details see supplementary material SM.3, figure SM4, available at stacks.iop.org/JPhysCM/23/315402/mmedia).

The temperature dependences of $|D|$ and $|E|$ obtained from the spectral simulations are presented in figure 5. For both samples, as temperature increases, $|D|$ decreases and $|E|$ increases. These temperature dependences are governed by two factors: static—related to the structural changes reflected in thermal expansion—and dynamic—related to the strength of the coupling between spins and phonons [29, 53]. In the case of fluorides these contributions are both expected to be

present and are expected to be equally important because the continuous structural distortions are strongly related to both thermal expansion and the dynamics of phonons. The shape of the temperature dependences of the ZFS is influenced by both factors. A detailed discussion of the temperature behaviour of the ZFS, in relation to the molecular dynamics, is given in section (chapter) 4.

The $Y \propto (A_C - X)^B$ formula (analogous to the equation describing the order parameter as a function of temperature in the ferroelectric phase) was used to fit $|D|$ versus T curves in the temperature range studied (figures 5(a) and (b)). The fitting curves obtained, despite lying in the range of experimental errors, do not sufficiently reflect the course of the dependence, which is especially evident for $BaZn_{0.999}Mn_{0.001}F_4$. $|D|$ versus T curves show subtle (at the limits of the experimental errors) changes in the course of the dependence from close to linear at higher temperatures to nonlinear at lower temperatures (figures 5(a) and (b)). Using the same fitting formula ($Y \propto (A_C - X)^B$) separately for the low and high temperature ranges (see the caption for figure 5 for details) significantly improves the agreement and demonstrates the two distinct characters of the dependence. For $BaZn_{0.999}Mn_{0.001}F_4$ the estimated temperature at which the change occurs is $\sim 300 \pm 20$ K whilst for $BaMg_{0.995}Mn_{0.005}F_4$ it is at $\sim 240 \pm 20$ K. Correspondingly, anomalies in the temperature dependence

of $|E|$ occur at $\sim 300 \pm 20$ K for $BaZn_{0.999}Mn_{0.001}F_4$ and $\sim 240 \pm 20$ K for $BaMg_{0.995}Mn_{0.005}F_4$ (figures 5(a′) and (b′)); this is in very good agreement with the change in the character of $|D|$. The most likely mechanism for these changes is related to the discontinuous changes in the geometry of the octahedra that are described in detail in section (chapter) 4.

The g factor and hyperfine interaction A_{iso}^{Mn} depend very weakly on temperature, with changes within the experimental errors.

3.3. Raman scattering

Depolarized Raman spectra recorded at room temperature for all the samples investigated are presented in figure 6. For group symmetry C_{2v}^{12} and four molecules in the unit cell, 33 Raman active modes are expected from group theory in the ferroelectric phase of $BaMF_4$ (M^{2+} = Mg^{2+}, Zn^{2+}, Co^{2+}, Fe^{2+}, Ni^{2+}, Mn^{2+}): $11A_1 + 6A_2 + 5B_1 + 11B_2$ [25, 33, 54]. In our experiments, for all materials investigated the total number of observed bands does not exceed 13, a situation which is not unusual with band overlap, low intensity bands and our spectral cut-off at 80 cm^{-1}, even though the symmetry assignment of the bands is difficult because of the depolarized nature of the spectra. However, all the observed bands are in good agreement with previously published data (for details see supplementary material SM.4, table SM1, available at stacks. iop.org/JPhysCM/23/315402/mmedia) [34, 37].

The observed phonon spectrum is a spectral signature of the structure of the fluorides studied and it is expected that the room temperature Raman spectra will have a similar pattern of bands for all members of the family, as well as for samples modified by doping, in agreement with our observation [34]. However, when comparing $BaMgF_4$ and the low level doped $BaMg_{0.999}Mn_{0.001}F_4$ and $BaMg_{0.995}Ni_{0.005}F_4$ it can be seen that the frequencies of some bands are affected by the chemical composition (see table SM1 in the supplementary material available at stacks.iop.org/JPhysCM/23/315402/mmedia), as observed earlier for Mn^{2+} doped $BaZnF_4$ [28]. For instance, the bands at ~ 258, 266 and 333 cm^{-1} in $BaMgF_4$ are shifted to higher frequencies in $BaMg_{0.999}Mn_{0.001}F_4$ (by approximately 0.3–2 cm^{-1}) but to lower frequency in $BaMg_{0.995}Ni_{0.005}F_4$.

Such a consistent trend for phonon frequencies in the doped samples is related to the level of structural distortion (which is induced by the large ionic radius) rather than the difference in the mass of the dopant as observed previously in [28]. This model is also consistent with our observation that even at very small levels of doping (0.1%) the shifts are dominated by the level of the distortion due to the differences between the ionic radii Mg^{2+} (r = 0.69 Å) < Zn^{2+} (r = 0.74 Å) < Mn^{2+} (r = 0.84 Å) rather than differences in the mass, Mg^{2+} (m = 23.98) < Mn^{2+} (m = 54.93) < Zn^{2+} ($m = 63.92$).

Some small differences in the amplitudes of the less intense bands between 150 and 190 cm^{-1} are observed, probably due to small differences in the orientation of the crystals between the various samples investigated.

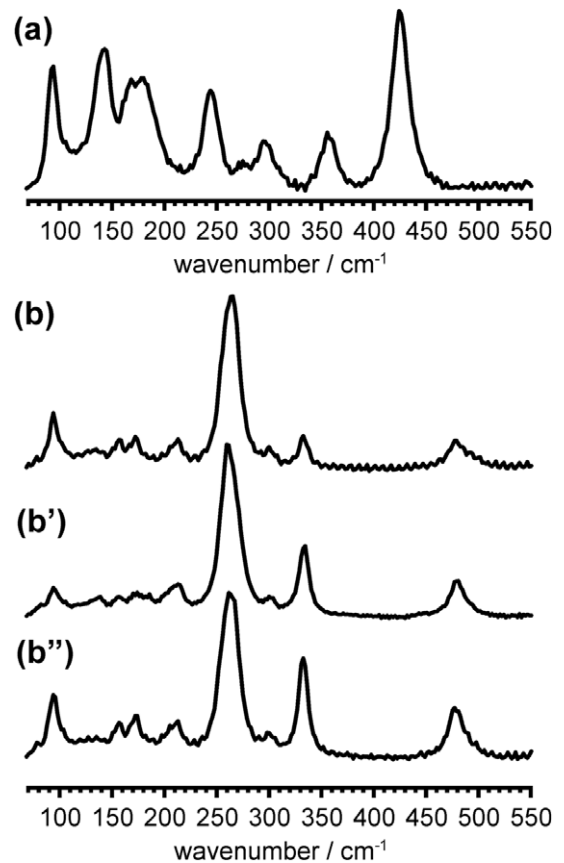Raman spectra were recorded for $BaZnF_4$ over a range of temperature and are presented in figure 7(a). The lowest

Figure 6. Depolarized Raman spectra of $BaZnF_4$ (a), $BaMgF_4$ (b), $BaMg_{0.999}Mn_{0.001}F_4$ (b′) and $BaMg_{0.995}Ni_{0.005}F_4$ (b″) recorded at room temperature for randomly oriented crystals.

temperature spectrum (83 K) is characterized by sharp bands with the most intense one at ~ 425 cm^{-1}. The expected trend of linewidth broadening and shift towards lower frequencies with increasing temperature is observed and this results in an increased band overlap. However, the bands at ~ 360 cm^{-1} and ~ 425 cm^{-1} (labelled A and B respectively in figure 7(a)) remain isolated over the whole temperature range. Such Raman bands at high frequencies are considered as particularly sensitive to small structural changes [28].

The temperature evolutions of the single-line bands A and B are represented in figure 7, by the dependences of the positions (figures 7(b) and (c)), integrated intensity ratios (figures 7(b′) and (c′)) and linewidths (figures 7(b″) and (c″)). As seen from figure 7, the spectral changes are very subtle and indicate that no major structural transition takes place. Nevertheless, we note slight anomalies at around 310 K which might indicate a local and subtle structural rearrangement related to changes in molecular dynamics. It is useful to stress that these anomalies occur in the temperature range for which we observed changes in the ZFS parameters. Earlier papers [25–28] also report spectral changes at approximately 170 K for low frequency bands in the $BaZnF_4$ spectrum, but the very subtle changes in our spectra at the same temperature are not evidence in themselves for any structural change.

Figures 8(a), 9(a) and 10(a) present, to the best of our knowledge, the first temperature-dependent Raman spectra
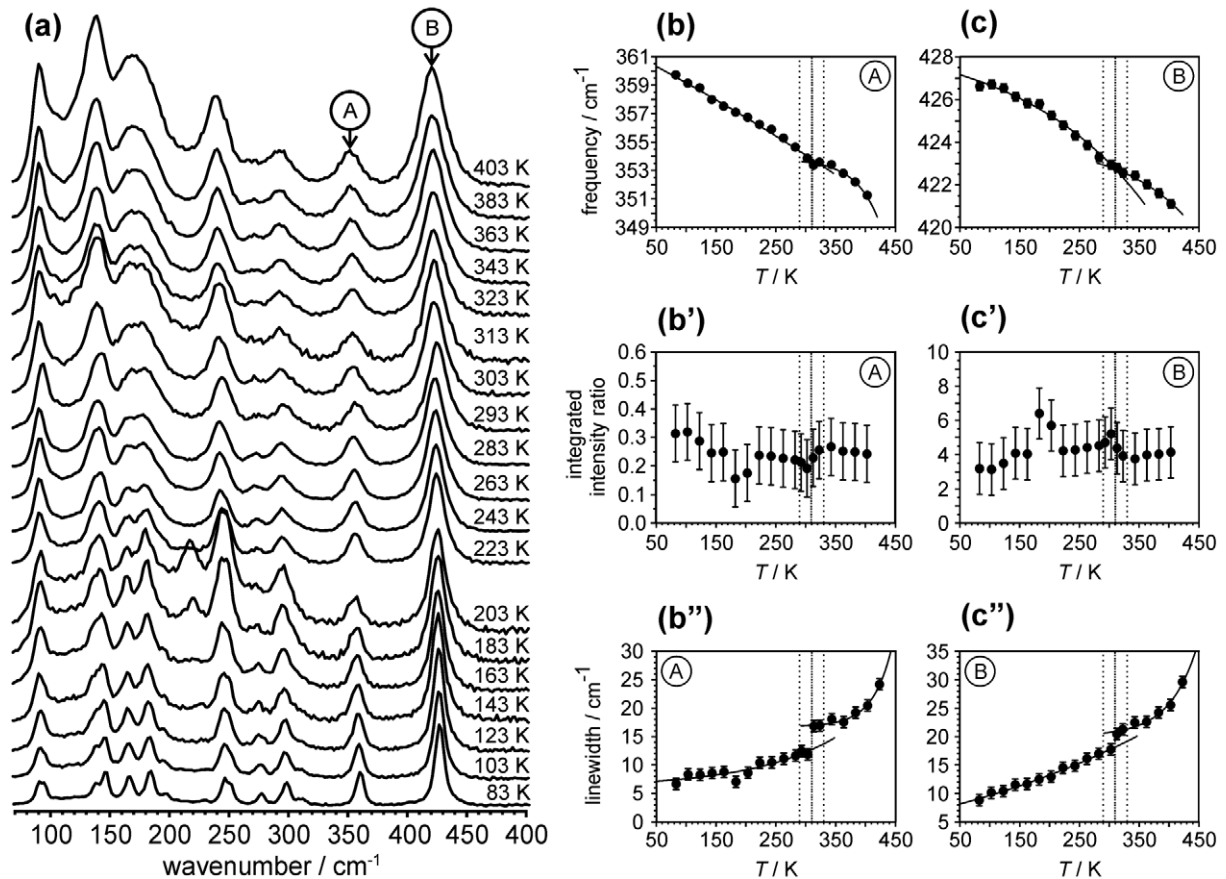
Figure 7. Variable temperature Raman spectra of BaZnF$_4$ (a). For clarity all spectra were normalized in reference to the amplitude of band A recorded at 83 K. Temperature dependences are shown for the frequencies ((b) and (c)), integrated intensity ratios ((b′) and (c′)) and linewidths ((b″) and (c″)) of the selected bands A and B. Solid lines are guides for the eye only. Vertical dotted lines indicate the temperature range in which the discontinuity occurs (marked by a bold dotted line).

of BaMgF$_4$, BaMg$_{0.999}$Mn$_{0.001}$F$_4$ and BaMg$_{0.995}$Ni$_{0.005}$F$_4$, respectively, in the range of 83–403 K. The variable temperature spectra of BaMgF$_4$ and BaMg$_{0.999}$Mn$_{0.001}$F$_4$ display very similar structures. The spectra for these two materials are well defined at low temperature with an intense doublet at ∼270 and ∼280 cm^{-1} which merges into a single band due to thermal broadening upon heating (figures 8(a) and 9(a)). The pattern of bands in the Raman spectrum of BaMg$_{0.995}$Ni$_{0.005}$F$_4$ resembles that of BaMgF$_4$ and BaMg$_{0.999}$Mn$_{0.001}$F$_4$, with a dominating central doublet, but some differences in the pattern of less intense bands are observed and attributed to possible small differences in the orientation of the crystals between samples.

As well as the similarities in both the patterns of bands and the temperature dependences, the Raman spectra of all three materials evolve with temperature continuously without drastic spectral changes, which would indicate a structural phase transition. Nevertheless, it has been shown previously that more detailed analysis of the spectra in terms of monitoring the positions, intensities and linewidths of different bands is useful for identifying more subtle structural rearrangements [37, 55]. Taking this into consideration, the temperature evolutions of the spectral characteristics for the selected bands of all three materials are presented in figures 8(b)–(c″), 9(b)–(c″)

and 10(b)–(c″). The choice of bands was guided by identifying isolated bands and considering in more detail high frequency bands which are often particularly sensitive to structural changes [28]. An illustration of this reasoning is the selection of the single-line band at ∼331 cm^{-1} for BaMgF$_4$ (labelled C in figure 8(a)) which remains well isolated across the whole temperature range. While this band has been analysed for all three samples, different additional bands have been selected depending on the actual spectral signature of the material.

The detailed spectral analyses illustrated in figures 8(b)–(c″), 9(b)–(c″) and 10(b)–(c″) provide corroborating evidence for subtle but significant spectral anomalies in the temperature range from 200 to 250 K. The observed anomalies are more or less pronounced, depending on the material and the band investigated. The identification of a critical temperature is dependent on the band and material under consideration. For example, for BaMgF$_4$ the most significant changes with the temperature occur in the band position, which is clear from the analyses of the selected bands C and D1 (figure 8). For the doped samples, BaMg$_{0.999}$Mn$_{0.001}$F$_4$ and BaMg$_{0.995}$Ni$_{0.005}$F$_4$ the spectral changes are more pronounced and are observed not only in the band positions, but also in the intensity ratios and linewidths, as illustrated in figures 9 and 10, respectively.
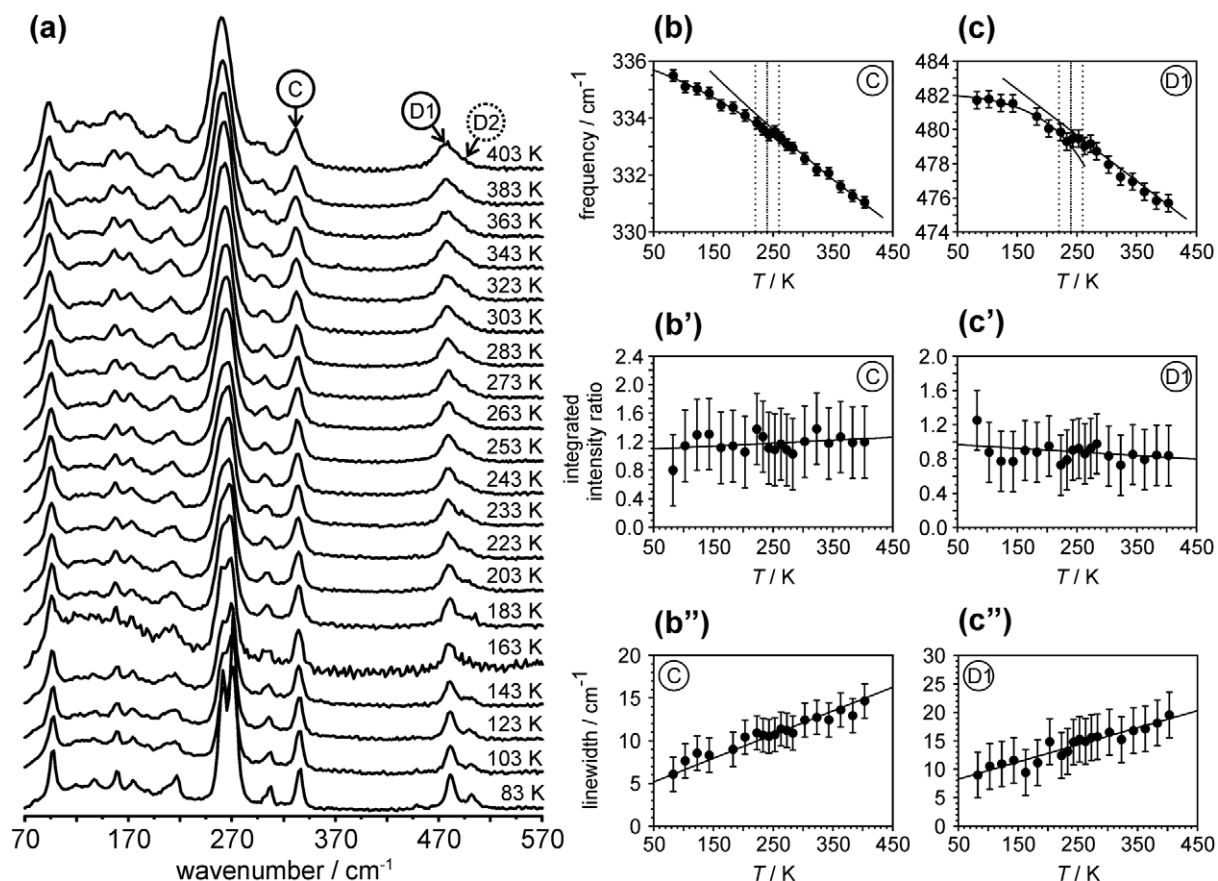
Figure 8. Variable temperature Raman spectra of BaMgF$_4$ (a). For clarity all spectra were normalized in reference to the amplitude of band C recorded at 83 K. Temperature dependences are shown for the frequencies ((b) and (c)), integrated intensity ratios ((b′) and (c′)) and linewidths ((b″) and (c″)) for selected bands C and D1. Solid lines are guides for the eye only. Vertical dotted lines indicate the temperature range in which the discontinuity occurs (marked by a bold dotted line). The temperature dependence of the spectral characteristic for band D2 is given in the supplementary material (available at stacks.iop.org/JPhysCM/23/315402/mmedia).

4. Analysis and discussion of the molecular dynamics of fluorides

To analyse in detail the variable temperature data obtained in this study it is necessary to recall the conclusion that for fluorides the unique structure shapes their molecular dynamics and ferroelectric properties [18, 20, 41]. Our multi-technique study provides information that can help to clarify and provide better understanding of the molecular dynamics of the fluorides studied. However, it is necessary to stress that the observed effects are very subtle, which reflects the high level of structural order in these materials and the high sensitivity and resolution of the experimental techniques, which have been achieved only recently [35–40]. Despite the subtle character of the observations, their consistency across multiple experimental techniques and various samples of BaMF$_4$ materials provides strong evidence in favour of the proposed changes in the structure.

The structure of BaMF$_4$ in the hypothetical paraelectric phase consists of corner-sharing fluoride octahedra, which form sheets perpendicular to the *b* direction (figure 11(a)) [18, 20, 41]. The M–F–M chains are linear along both the *c* and *b* directions (figure 11(a)) [18, 20, 41]. In the paraelectric phase, the octahedra do not have a highly symmet-

ric regular shape but are trapezoidal, as assumed in a realistic model of close packing (figure 11(a)) [20]. The transition from the paraelectric to the ferroelectric phase involves rotation and distortion of the octahedra from their initial configuration and this is accompanied by shifts of the Ba^{2+} and M^{2+} ions as shown schematically in figure 11(b) [20]. Such behaviour continues as the temperature is lowered, resulting in a more compact arrangement of ions and a gain of energy by the crystalline lattice (figure 11(b)) [20].

The paraelectric phase in BaMF$_4$ materials has never been observed directly because the Curie point is above the melting temperature [16]. However, the paraelectric–ferroelectric transition and its mechanism have been strongly evidenced by both experimental and theoretical studies [16, 20, 21, 24]. There is also strong experimental evidence of the existence of the 'soft' Raman bands which disappear at the Curie point [24, 34]. Previously published EPR data also predict the phase transition from the rotation pattern of the main axis of the ZFS tensor [33].

During further cooling, short-range interactions between ions (close packing) will slow down and finally prevent continuous rotation and continuous geometrical distortion of the octahedra by 'locking' their movement in the *cb* plane (figure 11(d)). The 'locking' point will strongly depend
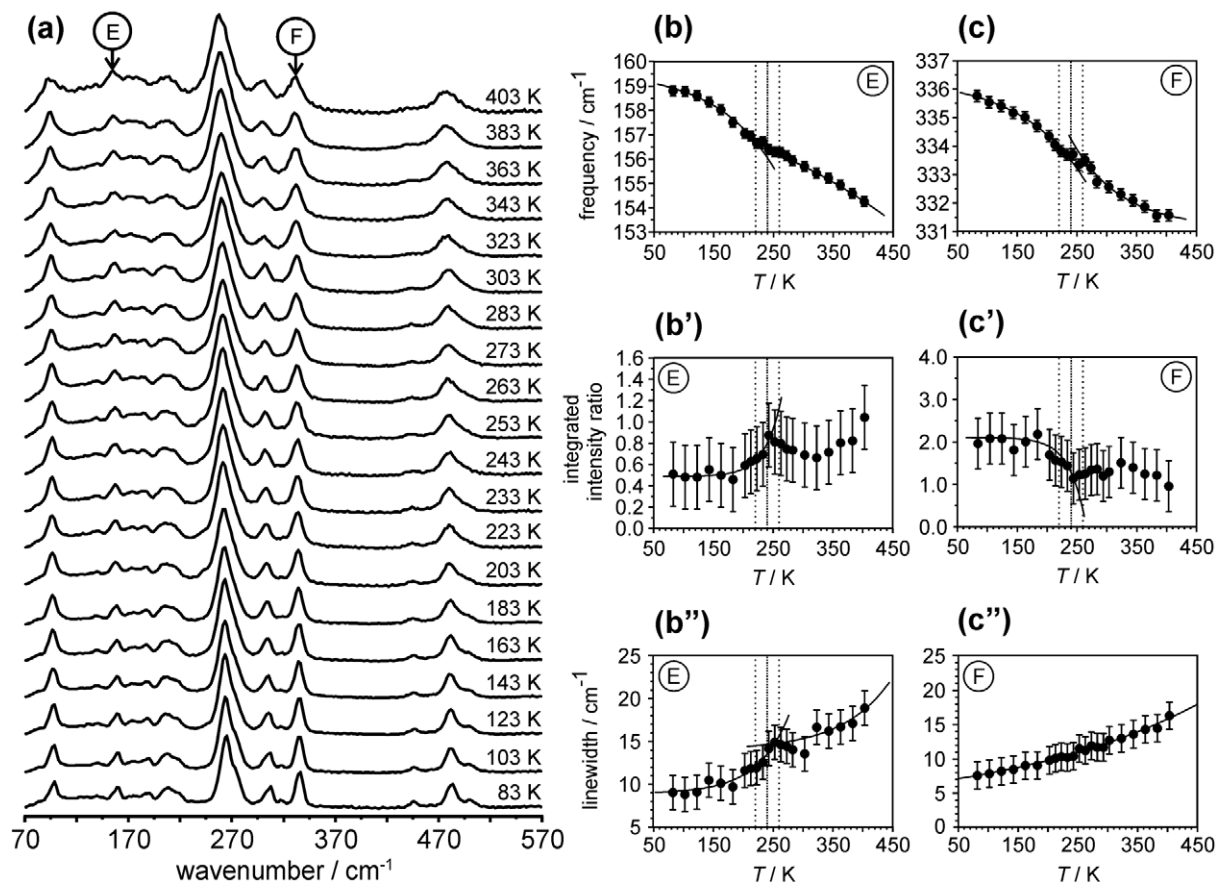
Figure 9. Variable temperature Raman spectra of $BaMg_{0.999}Mn_{0.001}F_4$ (a). For clarity all spectra were normalized in reference to the amplitude of band F recorded at 83 K. Temperature dependences are shown for the frequencies ((b) and (c)), integrated intensity ratios ((b′) and (c′)) and linewidths ((b″) and (c″)) for selected bands E and F. Solid lines are guides for the eye only. Vertical dotted lines indicate the temperature range in which the discontinuity occurs (marked by a bold dotted line).

on the size of the ion occupying the centre of octahedra because it determines the initial level of distortion at a given temperature. In this situation, to reduce the crystal energy further, the octahedra have to tilt around a new axis which is perpendicular to the *a* direction (figure 11(d)). Because such a change of rotation is not coherent over the whole sample, it initially induces disorder (dynamic clusters of librating octahedra) rather than a phase transition [25–28, 34]. For high levels of initial distortion, as observed only in $BaMnF_4$, a further decrease of temperature leads to the coherent rotation and the incommensurate–commensurate phase transition at 250 K [24].

Our data reflect the above consideration. The temperature dependence of the ZFS parameter $|D|$ (figures 5(a) and (b)) is strongly dependent on the molecular dynamics of the lattice because both thermal expansion and phonon contributions are present and approximately equally important [29, 53]. This assumption is justified in the case of geometric ferroelectric fluorides because both the thermal expansion and the dynamics of the phonons are strongly related to the unique structure and its dynamics which are manifested in rotation and continuous distortion of the octahedra.

In such a case, an increase of $|D|$ when reducing the temperature from 700 K to room temperature (figures 5(a)

and (b)) can be related to the rotation of the octahedra around the *a* axis and, associated with it, continuous small changes in the geometry (figure 11). This is supported by the corresponding decrease of $|E|$ (figures 5(a′) and (b′)), which implies that a more axial symmetry is prevalent at lower temperatures [56]. This continuous behaviour of $|D|$ and $|E|$ probably corresponds to the observed temperature dependence of the phonon frequency (figures 7–10).

At ~300 K for $BaZnF_4$ and 240 K for $BaMgF_4$, changes in the temperature dependences of $|D|$ and $|E|$ are observed (figure 5). The most likely mechanism of those changes is the discontinuous distortion of the geometry of the octahedra which originates in their rotation around a new direction (figure 11(c)). Additionally, below these temperatures, the form of the temperature dependences of $|D|$ and $|E|$ will change. These changes are due to the temperature dependence of the ZFS mechanism being more strongly dependent on the couplings with phonons than thermal expansion, which at lower temperatures is expected to be less efficient than at high temperatures [29, 53].

This discontinuous distortion mechanism is further supported by the ^{19}F MAS NMR data. The temperature dependence of the relative differences in the chemical shifts $\Delta\delta_{iso}^{ij}$ for $BaMgF_4$ (figure 3(b)) show discontinuities at
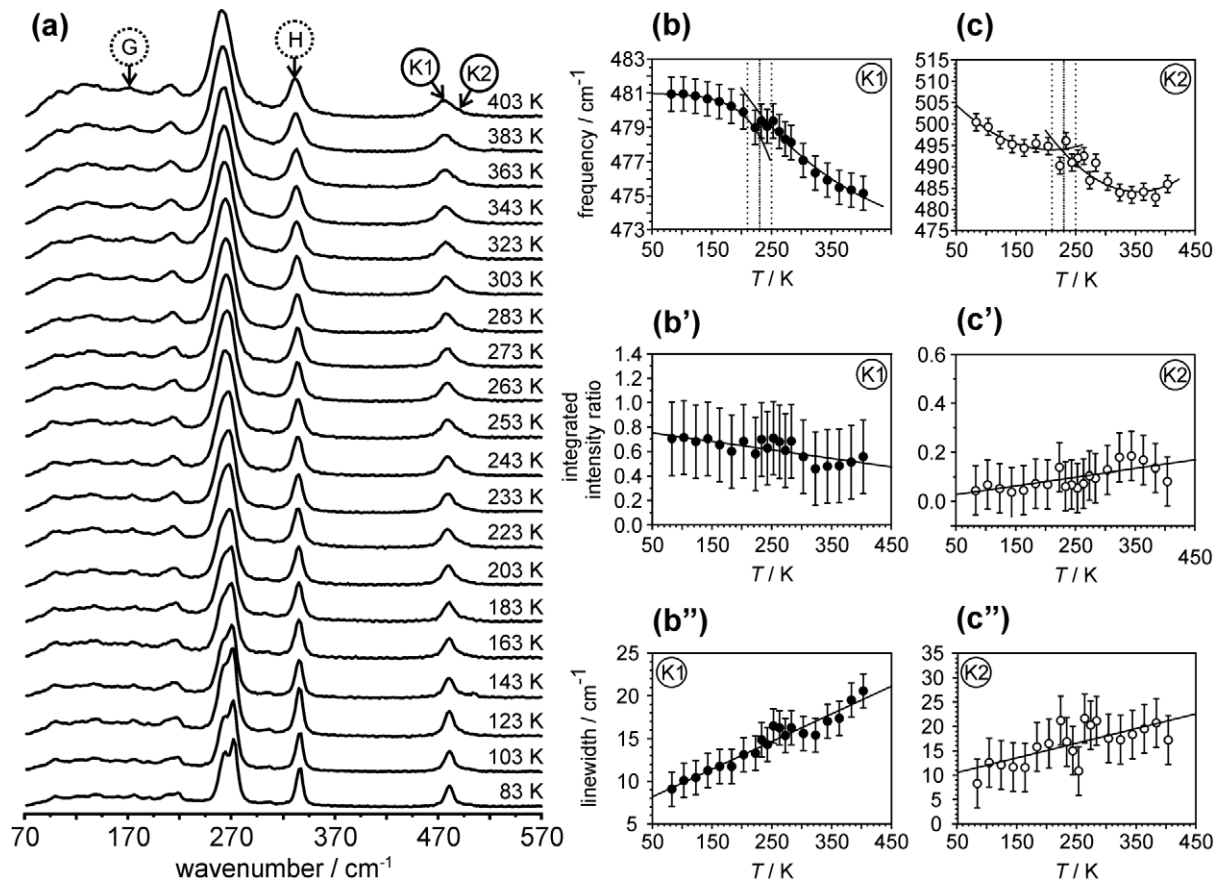
Figure 10. Variable temperature Raman spectra of $BaMg_{0.995}Ni_{0.005}F_4$ (a). For clarity all spectra were normalized in reference to the amplitude of band H recorded at 83 K. Temperature dependences are shown for the frequencies ((b) and (c)), integrated intensity ratios ((b′) and (c′)) and linewidths ((b″) and (c″)) for selected bands K1 and K2. Solid lines are guides for the eye only. Vertical dotted lines indicate the temperature range in which the discontinuity occurs (marked by a bold dotted line). The temperature dependences of the spectral characteristic for bands G and H are given in the supplementary material (available at stacks.iop.org/JPhysCM/23/315402/mmedia).

approximately the same temperature as the EPR data. These discontinuities are caused by a discontinuous change in the fluorine coordination sphere and can be directly related to a discontinuous change of the geometry of the fluorine octahedra. Since the main change involves F(1), F(2) and F(3) fluorine nuclei (with related changes in the bond lengths and their angles; figure 1) and is not related to continuous rotation, it is most likely that the origin of this discontinuous distortion is rotation of the octahedra about a new axis (figure 11(c)). The temperature of the observed change in the NMR data, 220 ± 20 K, corresponds, within experimental error, to the temperature at which changes in the ZFS parameters are observed (240 ± 20 K).

The Raman data are in agreement with this hypothesis and provide further evidence for the discontinuous distortion mechanism. Subtle anomalies in the frequency and linewidth of some of the high energy bands in $BaMgF_4$ (figure 8), $BaMg_{0.999}Mn_{0.001}F_4$ (figure 9), and $BaMg_{0.995}Ni_{0.005}F_4$ (figure 10) are observed between 200 and 250 K and reflect their sensitivities to small modifications to the geometries of the octahedra (see section 3.3). Such small changes in these geometries are not expected to have any significant effect on the softening or hardening of the bands related to their collective rotation around the *a* axis. Instead, they will have

a much more significant influence on the phonons related to the vibration of the atoms forming the octahedra and will be manifested as anomalies in the frequencies and possibly linewidths.

These observed anomalies cannot be explained by the presence of dopants or defects, because they have been observed for undoped ($BaMgF_4$; figure 8) and doped samples ($BaMg_{0.999}Mn_{0.001}F_4$ (figure 9) and $BaMg_{0.999}Ni_{0.001}F_4$ (figure 10)), with different levels of defects.

The observed difference in the temperatures at which the distortion occurs (300 K for $BaZnF_4$ and 240 K for $BaMgF_4$) also supports the relation with the geometry of the octahedra (compare figures 5, 7 and 8). This difference in the temperature can be related to the different ionic radii of Mg^{2+} and Zn^{2+} (0.69 Å and 0.74 Å, respectively) which cause different degrees of initial lattice distortion at the same temperature below the Curie point. For the more distorted structure (i.e. $BaZnF_4$) changes in the dynamics have to occur earlier, which is in agreement with the ~60 K observed difference between $BaZnF_4$ and $BaMgF_4$.

We believe that the observed change in the geometry allows the octahedra to rotate around a different, more favourable direction and as a result it could be a precursor of some form of ordering. Rotation about the *a* axis
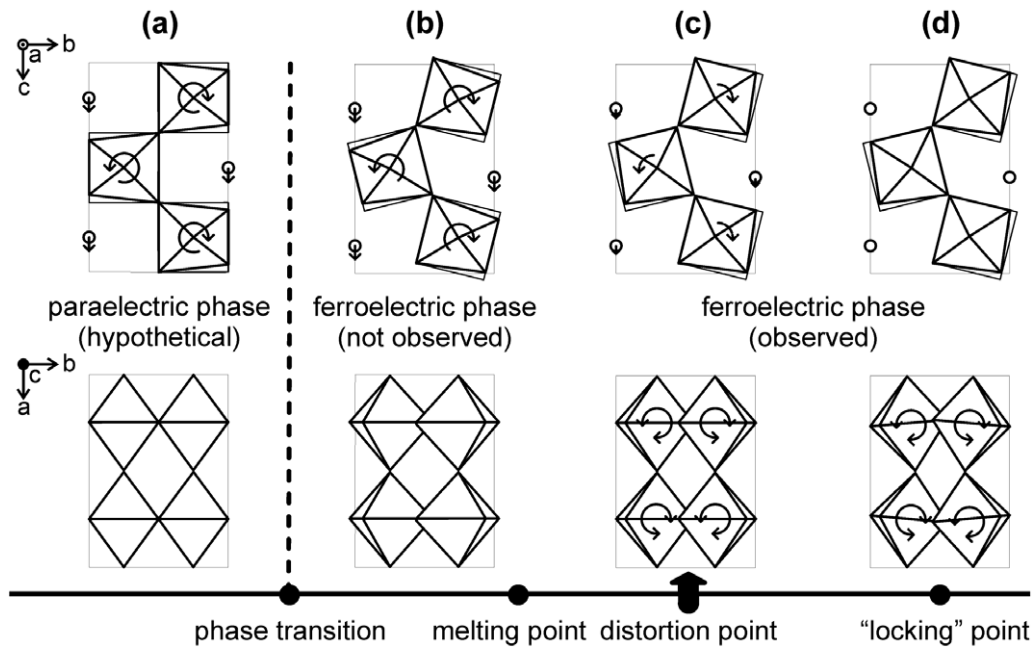
13

Figure 11. The schematic representation of the main structural changes in the fluorides: (a) the hypothetical paraelectric phase, (b) the ferroelectric phase above melting point, (c) the ferroelectric phase at which discontinuous structural distortion of octahedra occurs, (d) the ferroelectric phase at which rotation of octahedra is frozen. Arrows show the anticipated direction of structural changes.

still takes place, but with significantly less effect on the geometry of the octahedra, and finally stops, reaching a 'locking' point. Our suggested hypothesis is in agreement with the idea that the formation of the dynamic clusters is the precursor of the instability which leads to the doubling of the unit cell dimension along the *a* axis and a commensurate–incommensurate phase transition [25–28]. Such a phase transition is not observed in BaMgF$_4$ and BaZnF$_4$ because the level of lattice distortion is insufficient to force long-range ordering in the *ac* planes even at cryogenic temperatures. Only for BaMnF$_4$, where structural distortion is at its highest, in this family, can this mechanism lead to the well documented phase transition [24].

5. Conclusions

In these studies, we successfully applied magnetic resonance (NMR and EPR) techniques and Raman scattering to elucidate in detail the local nuclear and electronic structures as well as low temperature changes in the molecular dynamics of selected geometric ferroelectric fluorides.

The ^{25}Mg isotropic chemical shift δ_{iso}, quadrupolar coupling constants (C_q) and asymmetry parameters (η) reflect the distorted geometry of the Mg^{2+} octahedral coordination. For Mn^{2+}, which replaces Mg^{2+} during doping, the zero-field splitting parameters $|D|$ and $|E|$ are consistent with an octahedral coordination with a distorted axial symmetry at low temperatures and nearly rhombic symmetry at high temperatures. The observed high resolution of the NMR, EPR and phonon spectra are consistent with the highly ordered crystallographic structure.

By combining the temperature dependence data from multiple techniques, the subtle but important changes to the

zero-field splitting parameters $|D|$ and $|E|$, ^{19}F NMR isotropic chemical shifts and frequencies and linewidths of some high frequency Raman bands were shown to be consistent. The combined analyses provide strong evidence for discontinuous change with temperature in the structural distortion of the fluoride octahedra, which occurs at ∼300 K for BaZnF$_4$ and ∼240 K for BaMgF$_4$. This distortion allows the octahedra to rotate around a new axis which is approximately perpendicular to that related to the paraelectric–ferroelectric phase transition. The temperature at which this change occurs depends on the ionic radius of the central M^{2+} ion of the fluoride octahedra. The combined analysis also suggests that this geometrical change plays an important role in modifying the lattice dynamics as an initial step towards the creation of dynamic order in the structure.

spectrometer was purchased for an EPSRC (UK) Basic Technology Project, EP/D045967.

References

[1] Scott J F 2007 *Science* **315** 954–9
[2] Ziebowicz B, Szewieczek D and Dobrzanski L A 2007 *J. Achiev. Mater. Manuf. Eng.* **20** 207–10
[3] Egami T 2007 *Annu. Rev. Mater. Res.* **37** 297–315
[4] Eerenstain W, Mathur N D and Scott J F 2006 *Nature Mater.* **442** 759–65
[5] Hill N A 2000 *J. Phys. Chem.* B **104** 6694–709
[6] Fiebig M 2005 *J. Phys. D: Appl. Phys.* **38** R123–52
[7] Van Aken B B, Palstra T T M, Filippetti M A and Spaldin N A 2004 *Nature Mater.* **3** 164–70
[8] Ivanov V Y, Mukhin A A, Travkin V D, Prokhorov A S, Popov Y F, Kadomtseva A M, Voroblev G P, Kamilov K I and Balbashov A M 2006 *Phys. Status Solidi* **243** 107–11
[9] Lee S *et al* 2008 *Nature* **451** 805
[10] Fiebig M, Lottermoser Th, Kneip M K and Bayer M 2006 *J. Appl. Phys.* **99** 08E3021
[11] Sato T J, Lee S-H, Katsufuji T, Masaki M, Park S, Copley J R D and Takagi H 2003 *Phys. Rev.* B **68** 014432
[12] Scott J F and Blinc R 2011 *J. Phys.: Condens. Matter* **23** 113202
[13] Scott J F 1977 *Phys. Rev.* B **16** 2329–31
    Fox D L, Tilley D R, Scott J F and Guggenheim H J 1980 *Phys. Rev.* B **21** 2926–36
    Tilley D R and Scott J F 1982 *Phys. Rev.* B **25** 3251–60
[14] Fox D L and Scott J F 1977 *J. Phys. C: Solid State Phys.* **10** L329–31
[15] Ederer C and Spaldin N A 2006 *Phys. Rev.* B **74** 020401
[16] Eibschutz M, Guggenheim H J, Wemple S H, Camlibel I and DiDomenico M Jr 1969 *Phys. Lett.* A **29** 409–10
    DiDomenico M Jr, Eibschiitz M, Guggenheim H J and Camlibel I 1969 *Solid State Commun.* **7** 1119–22
    Ederer C and Spaldin N A 2006 *Phys. Rev.* B **74** 024102
[17] Bergman J G, Crane G R and Guggenheim H 1975 *J. Appl. Phys.* **46** 4645–6
    Asahi T, Tomizawa M, Kobayashi J and Kleemann W 1992 *Phys. Rev.* B **45** 1971–87
    Víllora E G, Shimamura K, Jing F, Medvedev A, Takekawa S and Kitamura K 2007 *Appl. Phys. Lett.* **90** 192909
    Tong Y, Meng X Y, Wang Z Z, Chena C and Lee M-H 2005 *J. Appl. Phys.* **98** 0335041
[18] Gingl F 1997 *Z. Anorg. Allg. Chem.* **623** 705–9
[19] Eibschtitz M and Guggenheim H J 1968 *Solid State Commun.* **6** 737–9
[20] Keve E T, Abrahams S C and Bernstein J L 1969 *J. Chem. Phys.* **51** 4928–36
    Keve E T, Abrahams S C and Bernstein J L 1970 *J. Chem. Phys.* **53** 3279–87
[21] Flocken J, Mo Z, Mei W N, Hardy J R and Hatch D M 1994 *Phys. Rev.* B **49** 5812–16
[22] Cox D E, Shapiro S M, Cowley R A, Eibschutz M and Guggenheim H J 1979 *Phys. Rev.* B **19** 5754–72
    Yoshimura M, Hidaka M, Mizushima T, Sakurai J, Tsuboi T and Kleemann W 2006 *J. Magn. Magn. Mater.* **299** 404–11
    Veira J R, Argyriou D N, Kiefer K, Wolter A U B, Alber D, Meissner M, Almairac R, Reehuis M and Bordallo H M 2008 *Phys. Rev.* B **78** 0541041
[23] Cox D E, Eibschutz M, Guggenheim H J and Holmes L 1970 *J. Appl. Phys.* **41** 943–5
[24] Scott J F 1979 *Rep. Prog. Phys.* **12** 1055–84
    Ryan J F and Scott J F 1974 *Solid State Commun.* **14** 5–9
    Bechtle D W, Scott J F and Lockwood D J 1978 *Phys. Rev.* B **18** 6213–29
    Lavrencic B B and Scott J F 1981 *Phys. Rev.* B **24** 2711–7
    Lockwood D J, Murray A F and Rowell N L 1981 *J. Phys. C: Solid State Phys.* **14** 753–72
    Ryan T W 1986 *J. Phys. C: Solid State Phys.* **19** 1097–106
    Sciau P, Lapasset J, Grebille D and Berar J F 1988 *Acta Crystallogr.* B **44** 108–16
    Yoshimura M and Hidaka M 2005 *J. Phys. Soc. Japan* **74** 1181–9
[25] Bordallo H N, Bulou A, Almairac R and Nouet J 1994 *J. Phys.: Condens. Matter* **6** 10365–76
[26] Almairac R, Bordallo H N, Bulou A and Nouet J 1995 *Phys. Rev.* B **52** 9370–6
[27] Almairac R, Bordallo H N, Bulou A, Nouet J and Currat R 1997 *Phys. Rev.* B **55** 8249–56
[28] Bordallo H N, Almairac R, Bulou A and Nouet J 1996 *J. Phys.: Condens. Matter* **8** 4993–5005
[29] Wan K L, Hutton S L and Drumheller J E 1987 *J. Chem. Phys.* **86** 3801–3
[30] Cai S-H, Yu X-Y, Chen Z and Wan H-L 2003 *Magn. Reson. Chem.* **41** 902–7
    Body M, Silly G, Legein C and Buzar J-Y 2005 *J. Phys. Chem.* B **109** 10270–8
    Zheng A, Liu S-B and Deng F 2009 *J. Phys. Chem.* C **113** 15018–23
[31] Recher K, Wallrafen F, Buscher R and Lehmann G 1981 *Phys. Status Solidi* b **107** 699–706
    Zhou Y-Y 1988 *J. Phys. C: Solid State Phys.* **21** 5547–53
    Dance J M, Boireau A, Le Lirzin A and Lestienne B 1994 *Solid State Commun.* **91** 475–9
[32] Rey J M, Bill H, Lovy D and Hagemann H 1998 *J. Alloys Compounds* **268** 60–5
    Yamaga M, Hattori K, Kodama N, Ishizawa N, Honda M, Shimamura K and Fukuda T 2001 *J. Phys.: Condens. Matter* **13** 10811–24
[33] Fukui M, Chikushi S and Abe R 1980 *J. Phys. Soc. Japan* **48** 1196–201
[34] Quilichini M, Ryan J F and Scott J F 1975 *Solid State Commun.* **16** 471–5
[35] Wind M, Saalwaechter K, Wiesler U-M, Muellen K and Spiess H W 2002 *Macromolecules* **35** 10071–86
[36] Krzyminiewski R, Bielewicz-Mordalska A and Kowalczyk R M 1998 *J. Magn. Reson.* **135** 76–81
[37] Bismayer U 1990 *Phase Transit.* **27** 211–267
[38] Bakhamutov V I 2010 *Chem. Rev.* **111** 530–62
[39] Cameron T S, Decken A, Kowalczyk R M, McInnes E J L, Passmore J, Rawson J M, Shuvaev K V and Thompson L K 2006 *Chem. Commun.* 2277–79
[40] Iliev M N, Litvinchuk A P, Abrashev M V, Popov V N, Cmaidalka J, Lorenz B and Meng R L 2004 *Phys. Rev.* B **69** 172301
    Girardot C, Kreisel J, Pignard S, Caillault N and Weiss F 2008 *Phys. Rev.* B **78** 104101
[41] Posse J M, Grzechnik A and Friese K 2009 *Acta Crystallogr.* B **65** 576–86
[42] Kunwar A C, Turner G L and Oldfield E 1986 *J. Magn. Reson.* **69** 124–7
[43] Bodart P R, Amoureux J-P, Dumazy J P and Lefort R 2000 *Mol. Phys.* **98** 1545–51
[44] Bak M, Rasmussen J T and Nielsen N C 2000 *J. Magn. Reson.* **147** 296–330
[45] Clark S J, Segall M D, Pickard C J, Hasnip P J, Probert M J, Refson K and Payne M C 2005 *Z. Kristallogr.* **220** 567–70
[46] Stoll S and Schweiger A 2006 *J. Magn. Reson.* **178** 42–55
[47] Gross U, Ruediger S, Grimmer A-R and Kemnitz E 2002 *J. Fluorine Chem.* **115** 193–9

[48] Bureau B, Silly G, Emery J and Buzaré J-Y 1999 *Chem. Phys.* **249** 89–104
[49] Bastow T J 2002 *Solid State Commun.* **124** 269–73
Freitas J C C, Wong A and Smith M E 2009 *Magn. Reson. Chem.* **47** 9–15
[50] Bleich H E and Redfield A G 1977 *J. Chem. Phys.* **67** 5040–7
Dupree R and Smith M E 1988 *J. Chem. Soc. Chem. Commun.* 1483–5
Bastow T J 1991 *Solid State Commun.* **77** 547–8
[51] Cahill L S, Hanna J V, Wong A, Freitas J C C, Yates J R, Harris R K and Smith M E 2009 *Chem. Eur. J.* **15** 9785–98

Widdifield C M and Bryce D L 2009 *Phys. Chem. Chem. Phys.* **11** 7120–2
[52] Yosida T, Aoki H, Takeuchi H, Arakawa M and Horai K 1991 *J. Phys. Soc. Japan* **60** 625–35
[53] Shrivastava K N 1969 *Phys. Rev.* **187** 446–50
Zheng W-C and Wu S-Y 1996 *Phys. Rev.* B **54** 1117–22
[54] Fukui M and Hirose T 1980 *J. Phys. Soc. Japan* **49** 1399–404
[55] Salje E K H and Bismayer U 1997 *Phase Transit.* **63** 1–75
Kreisel J, Glazer A M, Jones G, Thomas P A, Abello L and Lucazeau G 2000 *J. Phys.: Condens. Matter* **12** 3267–80
[56] Mabbs F and Collison D 1992 *EPR of Transition Metal Compounds* (Amsterdam: Elsevier)